Reference Network Construction for Persistent Scatterer Detection in SAR Tomography: Ant Colony Search Algorithm (ACSA)

Yang Huang, Xiaoxiang Zhu, Xiantao Wang, Zhen Dong, and Anxi Yu

***Abstract*—Synthetic aperture radar (SAR) tomography is a powerful multibaseline technique allowing to reconstruct volume structures by using datasets of the same area with slightly different viewing angles. Nowadays, the reference network technique (RNT) is widely applied in SAR tomography to detect single and double scatterers with no need for preliminary removal of atmospheric phase screen (APS). Therein, reference network (RN) construction as the basis of RNT is vitally important for effective APS calibration to successfully detect persistent scatterers (PSs) over the entire scene. Aiming at whole-scene PS detection, RN should be constructed with global distribution throughout the whole built environment. For the moment, standard RNT cannot achieve this goal because of the damage to network connectivity in the RN construction process. In this article, an ant colony search algorithm (ACSA) is designed for whole-scene RN construction via step-by-step exploring and retaining reliable single scatterers around each ant. The effectiveness of the proposed ACSA for RN construction is demonstrated through the three-dimensional SAR tomography experiments on high-resolution TerraSAR-X SAR data stack in Shenzhen, China.**

***Index Terms*—Ant colony search algorithm (ACSA), atmospheric phase screen (APS), reference network (RN), synthetic aperture radar (SAR) tomography.**

I. Introduction

DUE to the side-looking geometry of synthetic aperture radar (SAR) imaging [1], the layover problem that multiple scatterers are mapped onto the same pixel will inevitably be introduced, particularly in an urban environment characterized by densely spaced infrastructures. Layovers such as those between the ground and facade of nearby buildings or the rooftop of one building and the façade of a higher building in proximity occur ubiquitously. Persistent scatterer interferometry (PSI) [2]–[4] as an advanced remote sensing technique has the capability of detecting single scatterers via using a set of co-registered complex SAR images with small angular diversity. However, restricted by the assumption that there is at most one scatterer in each pixel, the pixels containing signal contributions from multiple scatterers, the so-called layovers, are typically discarded and cannot be detected in PSI processing. SAR tomography [5]–[9], as an extension of the PSI technique can form a synthetic aperture and thus it has the capability of distinguishing multiple scatterers interfering within the same resolution cell.

With the launch of advanced spaceborne SAR sensors with very high spatial resolution, such as TerraSAR-X/TanDEM-X and Cosmo-Skymed [12]–[14], brand new opportunities arise for tomographic mapping. For the moment, the data sets available for SAR tomography are acquired from repeat-pass spaceborne SAR systems. In repeat-pass mode, the humidity, temperature, pressure, and total electron content experienced by each acquisition varies in space and time. This inevitably incurs spatially and temporally variating atmospheric phase fluctuations, referred to as atmospheric phase screen (APS). According to previous studies [13], [14], the APS will fail the focus on tomographic imaging. Hence, it is regarded as the most relevant disturbance faced by SAR tomography and must be calibrated before scatterer detection.

A. Related Work

As described in [15], the APS can mainly be considered as a mixture of vertical stratification and horizontal turbulence components. More specifically, the former component (stratified APS) is highly correlated with topography variations, whereas the latter component (turbulent APS) is spatially correlated. In previous research works, great efforts have been made for APS calibration and methods can mainly be classified into the following three categories.

First, the APS can be retrieved and corrected with ancillary measurement data, such as multispectral data and meteorological data. The APS in each SAR image can be simply retrieved by integrated use of ancillary Moderate Resolution Imaging Spectroradiometer (MODIS) data [16], [17], GPS data [17]–[19], and weather forecasting products [20], [21]. It is a simple method for APS correction. The accuracy of the correction depends on the density of measurement stations. At present, it is tough to correct the APS with high accuracy on account of the sparse distribution of measurement stations. Nonetheless, with the gradual increase in the density of meteorological stations and GPS networks all over the world [22], [23], this method will be more and more accurate in the future.

Manuscript received February 17, 2022; revised April 19, 2022; accepted May 6, 2022. Date of publication May 23, 2022; date of current version June 14, 2022. This work was supported by the National Natural Science Foundation of China under Grant 61771478. *(Corresponding authors: Xiaoxiang Zhu; Xiantao Wang.)*

The authors are with the College of Electronic Science and Technology, National University of Defense Technology, Changsha 410073, China (e-mail: huangyang18@nudt.edu.cn; xiaoxiang.z@yahoo.com; wangxiantao18@nudt.edu.cn; dongzhen@nudt.edu.cn; yu_anxi@nudt.edu.cn).

Digital Object Identifier 10.1109/JSTARS.2022.3176498

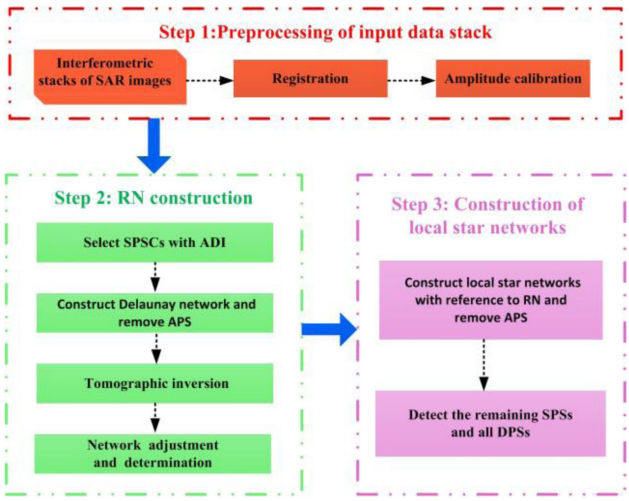

Fig. 1. Flowchart of standard RN technique for detecting SPSs and DPSs in SAR tomography.

Second, spatial-temporal filters can be applied to subtract APS. It is known that the topographic component and noise are highly correlated and uncorrelated in space and in time, respectively. Assuming that the APS is spatially correlated and temporally uncorrelated, the APS component can be subtracted by spatial low-pass and temporal high-pass filters [3], [24]–[27]. Successful APS subtraction relies on the setting of filtering parameters, such as the shape and length of the spatial-temporal filter. Excessive and incomplete filtering both prevents correct subtraction of APS contribution [28].

Third, the reference network (RN) technique [13], [14], [29], [30] can be exploited to cancel out the APS contribution with no need for preliminary removal of APS. Assuming that the APS difference between adjacent scatterers is small, the APS contribution can be considerably reduced by simply taking spatial phase differences between adjacent scatterers. With APS canceled out, the scatterers can be successfully focused in tomographic imaging and then be correctly detected. The longer the spatial distance between scatterers, the more uncertain the APS difference for the scatterers. For two scatterers with large spatial distances, there is a high probability that they have disparate APS distribution. For this reason, the distance threshold is introduced to control the APS uncertainty in RNT. The RNT can jointly detect single persistent scatterers (SPSs) and double persistent scatterers (DPSs) with no need for preliminary removal of APS, which avoids possible errors caused by uncertainty in spatiotemporal APS filtering and makes it more robust to monitor high-rise built environments. The flowchart of standard RNT is shown in Fig. 1 and the detailed processing steps are described as follows.

1) *Preprocessing of input SAR data stack*: SAR images are co-registered and one of them is chosen as the master image. Subsequently, the topographic phase contributions are simulated and removed with a reference digital elevation model (DEM).
2) *RN construction*: Delaunay triangulation is commonly used to connect the SPS candidates (SPSCs) selected with amplitude dispersion index (ADI) to generate the Delaunay network. The spatial phase difference is taken to cancel APS between connected SPSCs per arc. Thereafter, tomographic imaging is performed and relative parameters (elevation, displacement, and thermal dilation) are estimated for the connected SPSC pairs. Next, network adjustment is performed for the Delaunay network by only preserving reliable SPS pairs with high estimation precision. After network adjustment, isolated networks may yield and the largest one is chosen as RN. The RN constructed with standard RNT is called SRN in short. Finally, absolute parameters of the SPSs in SRN can be integrated relative to one reference SPS by the weighted least squares (WLS) estimator [14], [29]. In RN, only reliable SPSs with high estimation precision are preserved, which are used as reference points for detecting persistent scatterers (PSs) including SPSs and DPSs around them in the next step.
3) *Construction of local star networks*: Amplitude thresholding [3] is utilized to choose the PS candidates (PSCs). With the reliable SPSs as a reference, local star networks are constructed by connecting each PSC with its nearest SPS in RN. Likewise, the APS is canceled out by removing the phase of the reference SPS from the connected PSC for each arc in local star networks. Then, the remaining PSs including the remaining SPSs and all DPSs are detected from the RN-based local star networks. Parameters of the remaining PSs can be obtained by simply adding the corresponding values of reliable SPSs in RN.

Because there is no need for preliminary separation of APS in SAR tomography, the standard RNT has been widely used for robust detection of PSs since it was proposed. In this context, we will focus on the RNT for PS detection.

B. Research Gap

To detect PSs throughout the whole built environment, it is desired that RN should have whole-scene distribution over the entire built environment [29]. However, lots of arcs are discarded in the process of network adjustment for standard RNT. Therefore, the connectivity of the Delaunay network is damaged and isolated networks may yield. In this respect, the SRN by only utilizing the largest one will only cover part of the test area and other local regions that are not covered will lack reference points. As a result, PSs cannot be detected in the uncovered regions in the SRN-based local star networks.

In addition, SRN has another problem: In a complicated area with multiple overlaid structures, limited arcs with high estimation precision existed in the Delaunay network because of the big jump in height between connected SPSCs. Therefore, standard RNT has limited ability for preserving enough reliable SPSs in SRN. Then, it is difficult to retrieve the complete details of overlaid structures in a complicated area. In viewing the disadvantages faced by SRN, more research on RN construction with global distribution is required.

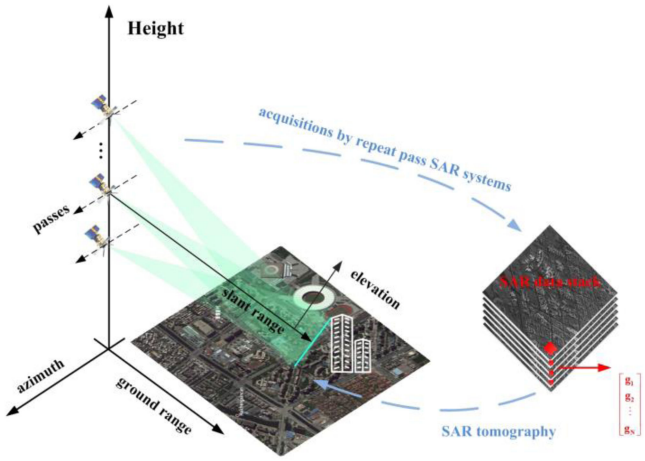

Fig. 2. Geometry of SAR tomography.

C. Contribution of This Article

To fill the aforementioned research gap, an ant colony search algorithm (ACSA) is proposed to construct RN with global distribution covering the whole built area. In ACSA, network connectivity is always maintained by step-by-step exploring and retaining reliable SPSs with high estimation precision around each ant until no reliable SPSs can be explored. Different from a freely connected network (FCN) [48], which refines the network after it is constructed, ACSA refines the network during its construction. This can explain that AntRN is a network with the near-largest coverage throughout the whole built environment.

The rest of this article is organized as follows. Section II gives a brief introduction to the signal model of SAR tomography. Besides, the method used for tomographic inversion and scatterer detection is reviewed. In Section III, the ACSA for RN construction is described. Finally, results are presented in Section IV and conclusions are drawn in Section V.

II. SAR Tomography

A. Tomographic SAR Imaging Model

For repeat-pass SAR systems, the geometry of classical three-dimensional (3-D) SAR tomography is depicted in Fig. 2 (the deformation and dilation term is ignored here for simplicity). The complex-valued measurement g_n at a given azimuth-range pixel of the nth acquisition from the registered SAR images can be modeled as [31]

$$g_n = \int_{\Delta s} \gamma(s) \exp(j2\pi\varepsilon_n s)\, ds \quad (n = 1, \ldots, N) \tag{1}$$

where $\gamma(s)$ denotes the reflectivity profile along slant elevation s. $\varepsilon_n = 2B_{n\perp}/\lambda r$ denotes the spatial frequency, which depends on the perpendicular baseline $B_{n\perp}$ of the $n$thacquisition, λ being the wavelength of the radar system, and r be the center slant range of the mater acquisition. It is seen that g_n can essentially be regarded as the Fourier transform of the elevation profile function $\gamma(s)$ of the observed scene at spatial frequency ε_n.

When APS is considered, (1) can be recast as

$$g_n = \int_{\Delta s} \gamma(s) \exp(j2\pi\varepsilon_n s + \phi_{\text{APS},n})\, ds \quad (n = 1, \ldots, N) \tag{2}$$

where $\phi_{\text{APS},n}$ represents the atmospheric phase delay experienced by the nth acquisition.

Model (2) can also be approximated as

$$\mathbf{g} = \mathbf{A}\gamma \tag{3}$$

where $\mathbf{g} = [g_1, g_2, \ldots, g_N]^T$ is the measurement vector ($[]^T$ is the transpose operator). $\boldsymbol{\gamma} = [\gamma_1, \gamma_2, \ldots, \gamma_M]^T$ is the reflectivity vector to be reconstructed. A is the mapping matrix with $A_{n,m} = \exp(j2\pi\varepsilon_n s_m)$, where $s_m (m = 1, \ldots, M)$ denotes the discrete elevation positions.

B. APS Cancellation

Assuming that there are at most two scatterers in an azimuth-range pixel, the SPS and DPS are involved. Then, three kinds of arcs, i.e., the SPS arc, SPS-DPS arc, and DPS-DPS arc, are considered. The SPS arc is the arc with two connected SPSs. The SPS-DPS arc is the arc consisting of an SPS and a DPS. The DPS arc is the arc with two connected DPSs.

1) SPS Arc: For the SPS arc, the measurement signal of the start SPS $\overset{\text{start}}{g}_n$ and the end SPS $\overset{\text{end}}{g}_n$ can be written as

$$\begin{cases} \overset{\text{start}}{g}_{\text{n}} = \overset{\text{start}}{A}_n \exp\left[j2\pi\varepsilon_n \overset{\text{start}}{s} + \overset{\text{start}}{\phi}_{\text{APS},n}\right] \\ \overset{\text{end}}{g}_{\text{n}} = \overset{\text{end}}{A}_n \exp\left[j2\pi\varepsilon_n \overset{\text{end}}{s} + \overset{\text{end}}{\phi}_{\text{APS},n}\right] \end{cases} \tag{4}$$

where $\overset{\text{start}}{s}$ and $\overset{\text{end}}{s}$ represent the elevation of the start SPS and the end SPS, respectively. $\overset{\text{start}}{A}_n$ and $\overset{\text{end}}{A}_n$ represent the complex scattering coefficients of the two connected SPSs on the SPS arc. Similarly, $\phi_{\text{APS},n}(i)$ and $\phi_{\text{APS},n}(j)$ represent the atmospheric phase delay experienced by two SPSs at the nth acquisition.

When the two SPSs are close in space, there is high possibility that they are affected with similar APS distribution

$$\overset{\text{start}}{\phi}_{\text{APS},n} \approx \overset{\text{end}}{\phi}_{\text{APS},n}. \tag{5}$$

Then the APS can simply be canceled out by subtracting the phase of $\overset{\text{start}}{g}_n$ from $\overset{\text{end}}{g}_n$. The differential signal Δg_n of the SPS arc after APS cancellation is given as

$$\Delta g_n = \frac{\overset{\text{end}}{g}_{\text{n}} \cdot \overset{\text{start}}{g^*}_{\text{n}}}{\left|\overset{\text{start}}{g}_{\text{n}}\right|} = \overset{\text{end}}{A}_n \exp(j2\pi\varepsilon_n \Delta s) \tag{6}$$

where $\Delta s = \overset{\text{end}}{s} - \overset{\text{start}}{s}$ represents the elevation difference of the two SPSs. For the SPS arc, the differential signal Δg_n has the signal model like a single scatterer when APS is effectively calibrated.

2) SPS-DPS Arc: Considering the SPS as the start point and the DPS as the endpoint, we have

$$\begin{cases} \overset{\text{start}}{g}_n = \overset{\text{start}}{A}_n \exp\left[j2\pi\varepsilon_n \overset{\text{start}}{s} + \overset{\text{start}}{\phi}_{\text{APS},n}\right] \\ \overset{\text{end}}{g}_n = \sum_{i=1}^{2} \left(\overset{\text{end}}{A}_n\right)_i \exp\left[j2\pi\varepsilon_n \overset{\text{end}}{s_i} + \left(\overset{\text{end}}{\phi}_{\text{APS},n}\right)_i\right] \end{cases}. \tag{7}$$

When the SPS and the two scatterers of DPS are adjacent in space, they have

$$\overset{\text{start}}{\phi}_{\text{APS},n} \approx \left(\overset{\text{end}}{\phi}_{\text{APS},n}\right)_i \quad (i = 1, 2). \tag{8}$$

For the SPS-DPS arc, the differential signal Δg_n has the signal model like the linear combination of two scatterers when APS is effectively calibrated.

3) DPS Arc: For the DPS arc, when the scatterers in the DPSs are close in space, similarly, we can cancel out the APS influence by subtracting the phase of the start DPS from the end DPS. Then, the differential signal Δg_n of the DPS arc can be written as

$$\Delta g_n = \frac{1}{\left|\overset{\text{start}}{g}_n\right|} \sum_{i=1}^{2}\sum_{j=1}^{2} \left(\overset{\text{end}}{A}_n\right)_j \cdot \left(\overset{\text{start}}{A}_n\right)_i \cdot exp\left(j2\pi\varepsilon_n \Delta s_{i,j}\right) \tag{9}$$

where $\Delta s_{i,j} = \overset{\text{end}}{s_j} - \overset{\text{start}}{s_i}$ denotes the elevation difference between the start DPS's ith scatterer and the end DPS's jth scatterer on the DPS arc. For the DPS arc, the differential signal Δg_n has the signal model alike the linear combination of four scatterers when APS is effectively calibrated.

According to the above analysis, the SPS arc, the SPS-DPS, and the DPS arc can be identified with a single peak, two peaks, and four peaks when APS is effectively canceled out, respectively. For the RN technique, the most reliable SPSs with high estimation precision are detected to form RN, and then the rest SPSs and all DPSs are detected in the RN-based local star networks. In other words, reliable SPS arcs with high estimation precision are identified to form RN. The SPS-DPS arcs and DPS arcs are identified to form local star networks.

C. Scatterer Detection

The goal of SAR tomography is to detect the PSs and acquire the corresponding parameters, such as the scatterer number, the elevation position and the complex scattering coefficient of each scatterer in PS. To fulfill this goal, tomographic inversion should be first conducted to reconstruct the reflectivity profile γ after APS cancellation. Thereafter, we can detect PSs through different scatterer detection strategies. For the moment, various methods have been proposed for tomographic inversion and scatterer detection, as demonstrated in [8] and [32]–[37]. For tomographic inversion, standard beamforming (BF) and compressive sensing are usually applied. For scatterer detection, generalized ratio test (GLRT)–based strategies [34]–[36] and model and information theoretic criteria based model order selection strategies [37], [38] are usually exploited.

For the moment, the BF-based sequential generalized ratio test with cancellation (BF-SGLRTC) algorithm [34] and the scale down by l_1 norm minimization, model order selection, and estimation refinement (SL1MMER) algorithm [37] are most commonly used for joint tomographic inversion and scatterer detection. BF-SGLRTC has the advantage of detecting SPSs with high efficiency. SL1MMER is known for its tremendous super-resolution ability for detecting DPSs at the cost of high computation burden. In this context, BF-SGLRTC is in RN used to detect the most reliable SPSs in RN. SL1MMER is used in local star networks, where DPSs are needed to be detected.

III. Proposed Algorithm: ACSA

The RN construction is essentially a problem of jointly detecting the most reliable SPSs and connecting them. It can essentially be regarded as a path-searching problem. As demonstrated in [39], the ant colony search (ACS) strategy inspired by the foraging behavior of real ants can get near-optimal solutions for various path-finding problems and has very wide applicability. Since it was proposed by Dorigo in 1992, a variety of algorithms have been developed for solving different kinds of natural problems, such as the traveling salesman problem [40], [41], the vehicle routing problem [42]–[44], and the network routing problem [45], [46]. To overcome the disadvantage faced by SRN, the intriguing ACS strategy is first applied and an ACSA is proposed in this article. As illustrated in Fig. 3, the detailed steps of ACSA are outlined as follows.

Outer iteration

Input: SPSCs;
If $N_{\text{rest}}/N < R_{\text{thres}}$
  Step 1: initialize start ant;
  proceed inner iteration from the start ant;
End
Step 6: RN determination;
Output: AntRN.

Inner iteration

Step 1: initialize the start ant
$\text{Ant} = \text{SPS}_C(\hat{i}), \hat{i} = \min_i(\text{ADI}_{\text{SPS}_C(i)}), (1 \le i \le N)$;
Step 2: connect per ant with its neighboring SPSCs:
$\text{arc}(p, j) = \{(p, j)|D[ant(p), SPS_C(j)] \le D_{\text{thres}}\}$;
Step 3: identify reliable SPS arcs:
$\text{arc}_{\text{SPS}}(p, \hat{j}) = \{(p, \hat{j})|\text{RSR}_{\text{arc}(p,j)} \ge \text{RSR}_{\text{thres}}\}$;
Step 4: control network redundancy by retaining at most K reliable SPS arcs with smallest arc distance around each ant;
Step 5: ant update: $\text{Ant} = \{\text{Ant}(p), \text{Ant}(q)\}$, $(1 \le q \le Q)$;
Stop when $Q = 0$.

Start (SPSC Preparation): Before RN configuration, the ADI threshold (normally not exceed 0.3) is used for the primary selection of SPSCs. Furthermore, the sparsification procedure

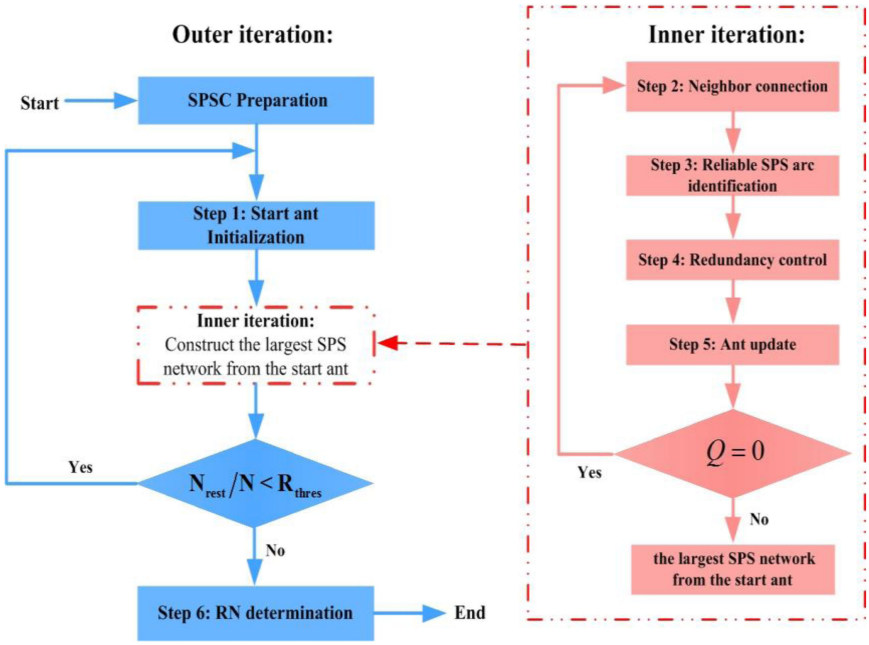

Fig. 3. Flowchart of ACSA for RN construction.

through placing a grid over the study site with appropriate cell width of $l_r \times l_a$ in the range-azimuth direction and preserving the SPSC with the smallest ADI in each grid cell is performed. This sparsification procedure has two advantages: 1) it can make the SPSCs more uniformly distributed throughout the whole built environment so that less computation and memory burden is needed for later processing; and 2) it increases the probability that the SPSCs are true SPSs.

Step 1 (Start Ant Initialization): Because all the PSs in the RN are SPSs, the start ant is desired to be a true SPS. The $\hat{i}$th SPSC with the smallest ADI is selected as the start ant, which is the most-likely true SPS. Assuming that N SPSCs are preserved after sparsification, the start ant is given as

$$\text{Ant} = \text{SPS}_C\left(\hat{i}\right), \hat{i} = \min_i \left(\text{ADI}_{\text{SPS}_C(i)}\right) \quad (1 \le i \le N) \tag{10}$$

where $\text{SPS}_C(i)$ represents the ith SPSC preserved after sparsification. $\text{ADI}_{\text{SPS}_C(i)}$ represents the ADI value of $\text{SPS}_C(i)$.

Step 2 (Neighbor Connection): Arcs are constructed via connecting per ant with its neighboring SPSCs. Distance threshold D_{thres} is predefined to increase the likelihood that the ant has similar APS distribution with the connected SPSCs on arcs. Assuming that there are P ants in this step, the constructed arc can be written as

$$\text{arc}\,(p,j) = \{(p,j)\,|D\,[ant\,(p)\,, SPS_C\,(j)] \le D_{\text{thres}}\} \tag{11}$$

where $Ant(p)$ represents the pth $(1 \le p \le P)$ ant. $SPS_C(j)$ represents the jth SPSC around $Ant(p)$, and $D[ant(p), SPS_C(j)]$ represents the distance between $Ant(p)$ and $SPS_C(j)$.

Step 3 (Reliable SPS Arc Identification): After arcs are constructed, the spatial phase difference is taken between the SPSC and the ant to remove the APS per arc. The BF-SGLRTC algorithm is then employed to detect SPS arcs from all arcs constructed in Step 2. In addition, the residue-to-signal ratio (RSR) threshold is used here to identify the most reliable SPS arcs with high estimation precision from the detected SPS arcs. With $\text{Ant}(p)$ as reference, reliable SPS arcs $\text{arc}_{\text{SPS}}(p,j)$ identified can be given as

$$\text{arc}_{\text{SPS}}\left(p,\hat{j}\right) = \left\{\left(p,\hat{j}\right)\left|\text{RSR}_{\text{arc}(p,j)} \ge \text{RSR}_{\text{thres}}\right.\right\} \tag{12}$$

where $\text{RSR}_{\text{arc}(p,j)}$ represents the RSR value of $\text{arc}(p,j)$. The constant $\text{RSR}_{\text{thres}}$ is usually set to be below 0.3. Meanwhile, relative elevations of the reliable SPS arcs can be obtained. In [15], RSR is given as

$$\text{RSR} = \frac{\sum_{n=1}^{N} |\Delta g_n - \Delta \hat{g}_n|^2}{\sum_{n=1}^{N} |\Delta g_n|^2} \tag{13}$$

where $\Delta \tilde{g}_n$ represents the estimated differential signal for an arc, with the following mathematic model:

$$\Delta \hat{g}_n = \begin{cases} \tilde{A} \exp\left(j2\pi\varepsilon_n \Delta\hat{s}\right), & \text{for SPS arc} \\ \sum_{i=1}^{2} \tilde{A}_i \exp\left(j2\pi\varepsilon_n \Delta\hat{s}_i\right), & \text{for SPS} - \text{DPS arc} \\ 1, & \text{otherwise} \end{cases} \tag{14}$$

where $\Delta\hat{s}$ denotes the estimated relative elevation between the connected SPSs if an arc is identified as an SPS arc. If an arc is identified as an SPS-DPS arc, $\Delta\hat{s}_i$ $(i = 1, 2)$ denotes the estimated relative elevation between the SPS and the ith PS of the DPS. The smaller the RSR value is, the higher precision the SPS arc is estimated. The quality of the estimates can also be related to phase deviation [36].

Step 4 (Redundancy Control): Since exhaustive explorations of all reliable SPS arcs around each ant are conducted, enormous reliable SPS arcs are identified in Step 3. Without control, the SPS network will be fairly redundant. Consequently, huge computation and memory burden will be brought for later processing. To control the network redundancy at an appropriate level, redundancy threshold K (normally above 3) is predefined and the procedure that at most K reliable SPS arcs with smallest arc distance are retained around each ant from the identified reliable SPS arcs is conducted. The reason we retain arcs with the smallest arc distance is that a longer arc distance means higher APS uncertainty for the connected SPSs. At the same time, the number of Q end SPS points, $\mathrm{SPS}(q)\ \ (1 \le q \le Q)$, on the final retained SPS arcs are also retained. Assuming that J reliable SPS arcs are identified with the pth ant as reference in Step 3, the retained reliable SPS arcs can be given as

$$\mathrm{arc}_{\mathrm{reliaSPS}}(p,k) = \begin{cases} \mathrm{arc}_{\mathrm{SPS}}\left(p,\hat{j}\right), & \text{if } J < K \\ \min_{1,\ldots,K} D\left[\mathrm{arc}_{\mathrm{SPS}}\left(p,\hat{j}\right)\right], & \text{if } J \ge K \end{cases}$$
$$\left(1 \le \hat{j} \le J, 1 \le k \le K\right) \tag{15}$$

where $\min_{1,\ldots,K} D[\mathrm{arc}_{\mathrm{SPS}}(p,\hat{j})]$ represents the operation of retaining K arcs with the smallest distance. In this step, the network redundancy can be well-controlled at the desired level K.

Step 5 (Ant Update): We update the ant(s) with the newly retained end SPS points in Step 4 and turn to Step 2 to continue the inner iteration. The updated ants can be given as

$$\mathrm{Ant} = \mathrm{Ant}p, \mathrm{Ant}q,\ 1 \le q \le Q \tag{16}$$

where Ant$p$ and Ant$q$ represent the reference ant and the newly retained end SPS in Step 4.

This inner iteration which cycles from Step 2 to Step 5 will end until no more reliable SPS arcs can be explored and retained starting from anyone of the ants. After the inner iteration, the largest SPS network with well-controlled redundancy can be constructed from the initial start ant. The rest N_{rest} SPSCs are updated by discarding the reliable SPSs in the SPS network. However, it is possible that this SPS network only covers a small area of the test site. To avoid this problem, threshold R_{thres} of the rest SPSCs to the total SPSC ratio is introduced. If $N_{\mathrm{rest}}/N \ge R_{\mathrm{thres}}$, we turn back to Step 1 to initialize another start ant from the rest SPSCs and start a new inner iteration. The outer iteration will end until $N_{\mathrm{rest}}/N < R_{\mathrm{thres}}$

Step 6 (RN Determination): Generally, we can acquire at least one SPS network through the above-mentioned steps. Each of them is the largest SPS network that could be constructed from one certain start ant. The one with the largest network coverage rate of the scene (NCRS) is determined as the final RN, called AntRN.

Considering that network is normally irregularly distributed in most cases, it is hard to directly calculate the network coverage area. Instead, the number of connected reliable SPSs N_{SPS} in the SPS network to the total SPSC ratio can be used to approximate NCRS

$$\mathrm{NCRS} = \frac{N_{\mathrm{SPS}}}{N}. \tag{17}$$

A larger NCRS implies wider network coverage.

The ACSA is an iterative algorithm, which cycles through step-by-step exploring and retaining reliable SPS arcs around each SPS from the start ant. There are two kinds of iterations in ACSA: 1) Inner iteration: step-by-step retaining reliable SPS arcs to the SPS network from one certain start ant; 2) Outer iteration: construct different largest SPS networks from different start ants. The inner iteration is iteratively performed in the outer iteration with different start ants.

Note that the proposed ACSA has the following three prominent advantages.

1) Network connectivity is always maintained in the construction process of ACSA by step-by-step exploring and retaining reliable SPSs in AntRN until no more reliable SPSs can be explored. This can explain that AntRN is a network with the near-largest coverage throughout the whole built environment.
2) Since exhaustive exploring for reliable SPSs around each ant is conducted in ACSA, the detailed structure information can be well retrieved in complicated areas where multiple structures overlap.
3) Redundancy threshold is predefined so that the network redundancy of ACSA can be well controlled.

Without control, the SPS network will be a fairly redundant network like FCN. Consequently, huge computation and memory burden will be brought for later processing. In practical application, the network redundancy of ACSA can be set flexibly according to the specific application requirements.

IV. Results

To validate the proposed ACSA for effective RN construction, a dataset of 26 high-resolution SAR images in staring spotlight mode acquired by TerraSAR-X over the Baoan district, Shenzhen, China has been considered. The data stack is acquired from January 5, 2016 to November 30, 2016 with a nominal revisiting period of 11 days, which has a slant range resolution of 0.6m and an azimuth range resolution of 0.24 m. Fig. 4 presents the mean-intensity image of the study site of interest. The SAR images used here are of HH polarization. We choose the SAR image acquired at July 10, 2016 as the master and the corresponding imaging parameters are displayed in Table I. As visible in Fig. 5, the span of the spatial and temporal baselines is approximately 357.2 m and 0.9 year, respectively. The spatial perpendicular baselines are non-uniformly distributed and are highly uncorrelated with the temporal baselines. Due to the short observation time span, the displacement is ignored and 3D SAR tomography model is used in this experiment for simplicity. Before PS detection, ADI threshold of 0.20 is used here for the primary selection of 63615 SPSCs. Moreover, sparsification with the grid cell width of 3×10 in the range-azimuth direction is placed in the scene and 14144 SPSCs are finally chosen for later RN construction (see Fig. 6).

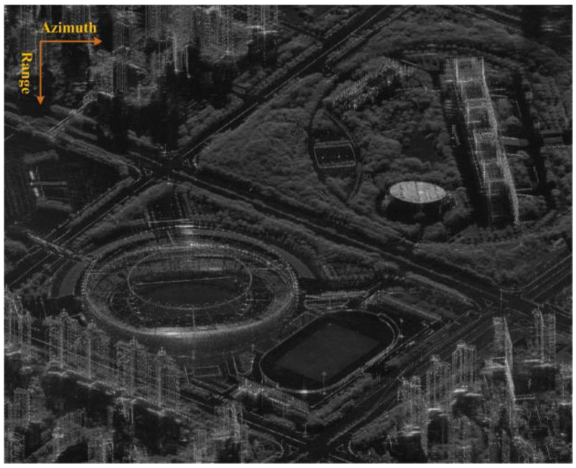

Fig. 4. Mean-intensity map from 26 SAR images of an urban area over Shenzhen (Size: 1376 × 3826 in the range-azimuth direction).

TABLE I
IMAGING PARAMETERS OF THE MASTER ACQUISITION

Imaging Parameters	Values
Orbit Direction	Descending
Orbit Height	688.58 km
Incidence Angle	39.48°
Polarization	HH
Carrier Frequency	9.65 GHz
Chirp Bandwidth	300 MHz

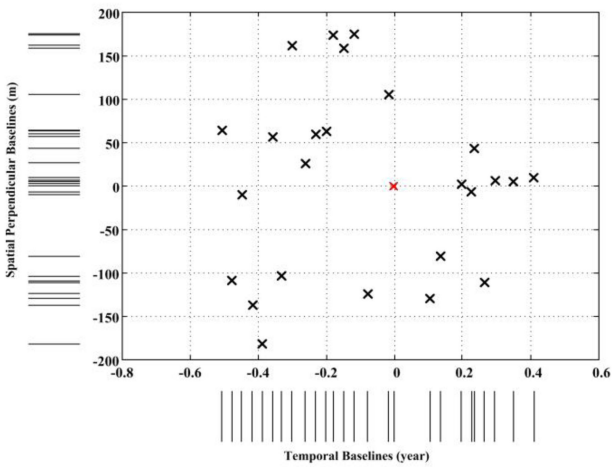

Fig. 5. Distribution of temporal and spatial perpendicular baselines. The master acquisition is marked with red color.

A. Construction of SRN and AntRN

All of the experiments are conducted on a PC with Intel Core i9-9820X CPU and 128-GB memory using MATLAB. Different methods, standard RNT and ACSA, are applied for constructing RN and then detecting SPSs and DPSs in the test site. The arc distance threshold D_{thres} of 300 m and the RSR threshold $\text{RSR}_{\text{thres}}$ of 0.25 are both taken for standard RNT and ACSA. In addition,

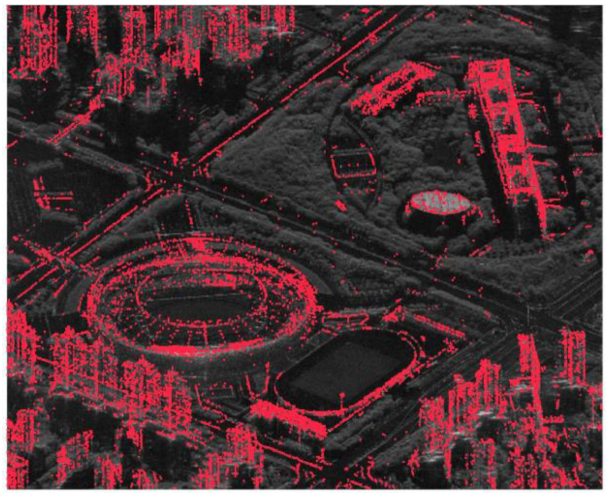

Fig. 6. Selected SPSCs (red solid dots) with a uniform distribution over the whole built environment. They are visualized in the mean-intensity map.

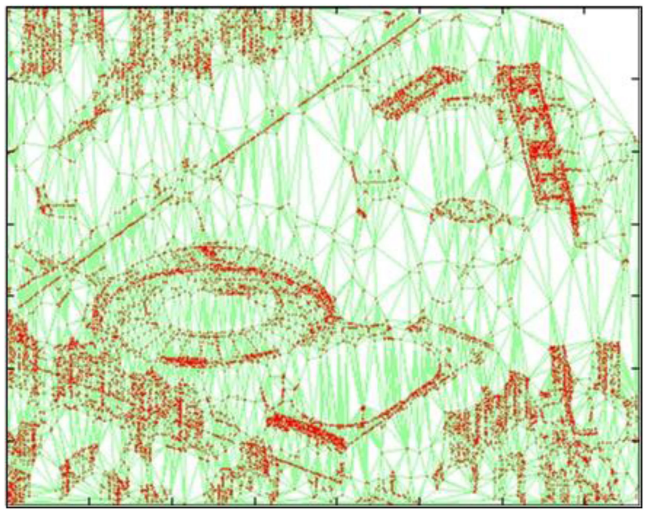

Fig. 7. Initial Delaunay network after repeat edge merging.

the redundancy threshold K used in ACSA is predefined to be 3 in this context so as to be consistent with the redundancy of SRN. With the columns in dictionary $\mathbf{A}$ be 312, the CPU time for the construction of SRN and AntRN is 848.02 and 5260.12 s, respectively. Since BF-SGLRTC is efficient, SRN and AntRN can both be constructed with high efficiency. The higher computation of SRN construction is caused by the searching of the largest connected network after network adjustment, which is no needed in AntRN construction.

The Initial Delaunay network after repeat edge merging is shown in Fig. 7. The constructed SRN and AntRN are shown in Fig. 8. The SRN consists of 17361 reliable SPS arcs and 7294 SPSs. The AntRN consists of 40026 reliable SPS arcs and 13805 SPSs. Compared with SRN, it is obvious that more reliable SPSs can be preserved in AntRN under the same condition. More specifically, many structures in Area 1 and Area 2 are not covered by SRN but are covered by AntRN. Besides, the line targets on road in Area 3 are not covered by SRN, but are well covered by AntRN. The whole scene of AntRN benefits

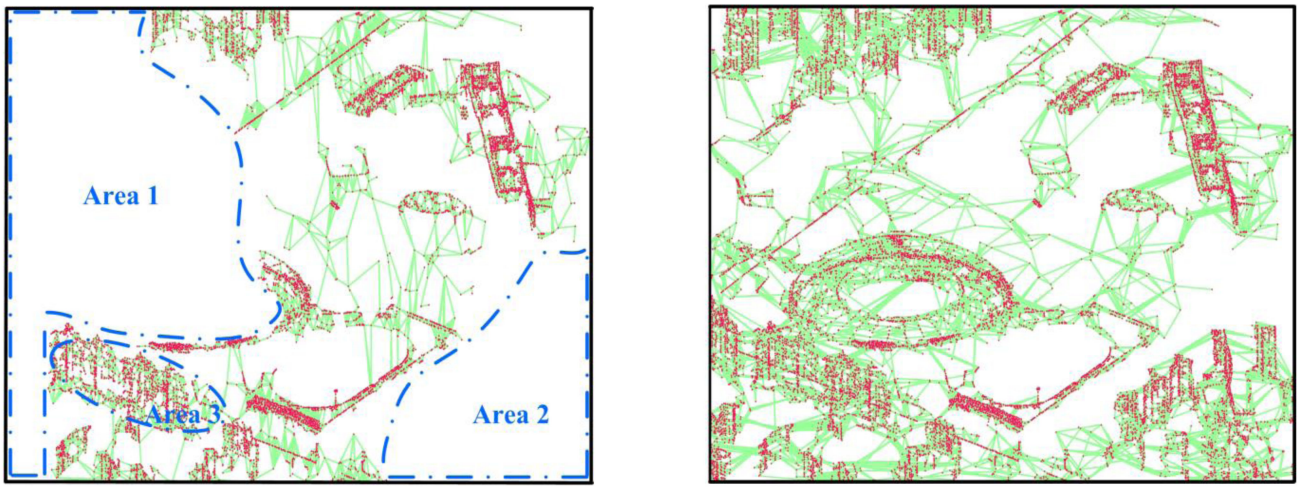

Fig. 8. Distribution of the constructed SRN (left) and AntRN (right). Area 1, Area 2, and Area 3 are the urban built areas that are not covered by the SRN. For both the SRN and the AntRN, the SPS arcs are marked with bright green lines and the SPSs are marked with red solid dots.

TABLE II
PS DETECTION WITH SRN AND ANTRN

Parameters	SRN	AntRN	Increase rate
Number of selected SPSCs	14 144	14 144	0
Number of SPSs in RN	7294	13 805	89.2%
Number of SPS-arcs in RN	17 361	40 026	130.6%
NCRS	0.516	0.976	89.2%
Number of PSCs	353 747	353 747	0
Total number of SPSs identified in local star networks	125 797	211 041	68.9%
Total number of DPSs identified in local star networks	17 630	30 781	74.6%
Total number of detected PSs	150 721	255 627	69.7%

from the capability of maintaining network connectivity at all times and stepwise exploring reliable SPSs exhaustively around each ant until no reliable SPSs can be explored in ACSA. For SRN, the lack of reliable SPSs in Area 1 and Area 2 is caused by network adjustment. The lack of enough reliable SPSs in Area 3 for SRN is because standard RNT has limited construction ability of reliable SPS arcs in a complicated area.

To quantitatively evaluate the coverage of SRN and AntRN, the NCRS value is additionally calculated (see Table II). The NCRS value of AntRN is 0.976 near 1. It means that the built area of the test site is completely covered by AntRN. In addition, it shows that 97.6% of the selected SPSCs are true SPSs, which validates the effectiveness of ADI threshold and sparsification procedure. In contrast, the NCRS value of CRN is 0.516, which illustrates that only part of the test site is covered by SRN. Compared with SRN, the NCRS value of AntRN has been increased about 89.2%. In this respect, we can conclude that ACSA has a greater ability for constructing RN with global distribution throughout the whole built environment.

Next, the WLS estimator is utilized to integrate the relative elevations and then retrieve the absolute elevations (relative to one reference point) for the detected reliable SPSs in SRN and AntRN. In this experiment, one SPS on the road, marked as white star, is set as the reference point with zero elevation at the test site. Fig. 9 presents the estimated absolute heights (with elevation transformed into vertical height) of the SPSs in SRN and AntRN. The smooth gradation of the estimated heights in the SRN and AntRN validate the correctness of the estimates. In addition, the consistency of the estimated heights for the SPSs in the SRN and AntRN also proves the correctness of the estimates

B. Construction of SRN-Based and AntRN-Based Local Star Networks

After RN is constructed, an amplitude threshold of 100 is adopted and 353 747 PSCs are selected. Then, as displayed in Fig. 10, the SRN-based local star networks and the AntRN-based local star networks are constructed with reference to SRN

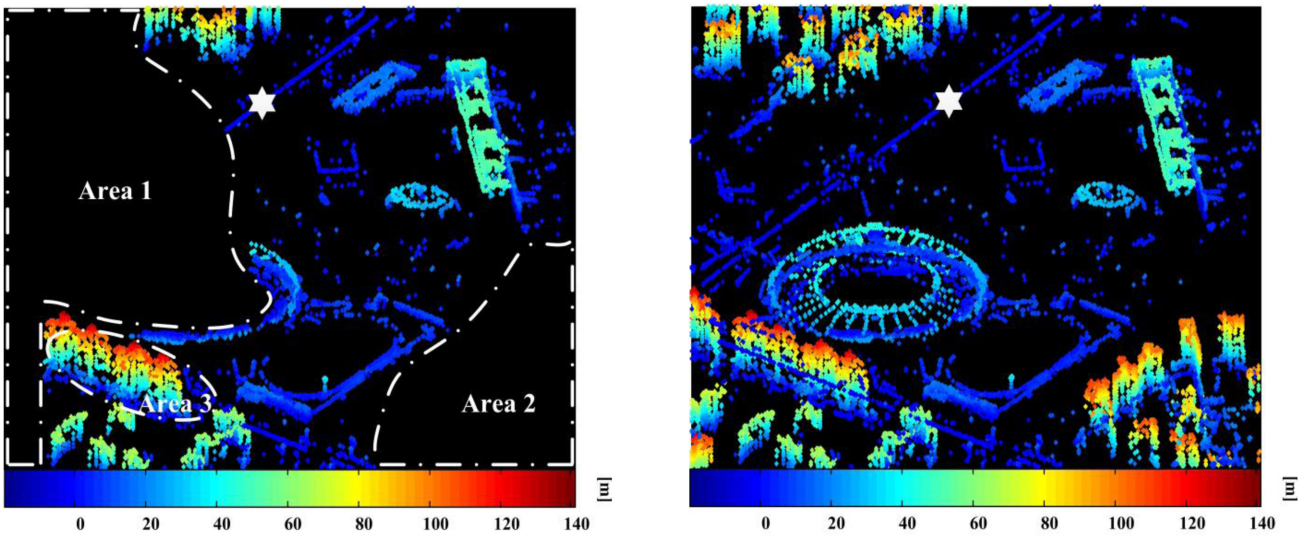

Fig. 9. (Left) Height map of the SPSs in SRN. (Right) Corresponding result of AntRN. The white star is the reference zero height point set in the test site. Area 1, Area 2, and Area 3 are the same area as shown in Fig. 7 (left).

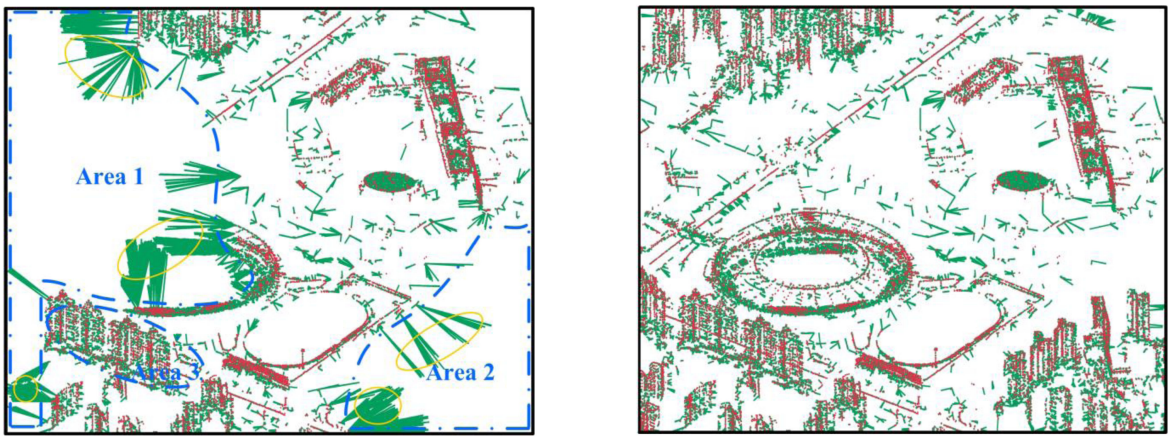

Fig. 10. (Left) SRN-based local star networks and (Right) AntRN-based local star networks. The red solid dots are the same SPSs shown in Fig. 8. The arcs of local star networks are marked with dark green lines. Area 1, Area 2, and Area 3 are the same area as shown in Fig. 8 (left).

and AntRN, respectively. Since there are no reference points at Area 1 and Area 2 for SRN [see Fig 8(left)], the construction of SRN-based local star networks in these areas is impossible, as displayed in Fig. 10 (left). It is seen that only a few small pieces of areas, marked with yellow circles, are covered by the SRN-based local star networks and most of the Area 1 and Area 2 cannot be covered. In addition, the line targets on road in Area 3 are not covered by SRN-based local star networks due to the lack of enough reference points in this area. In contrast, due to the global distribution capability of AntRN, the AntRN-based local star networks cover the entire built scene including Area 1, Area 2, and Area 3, as displayed in Fig. 10 (right).

In the SRN-based local star networks, 125797 SPSs and 17630 DPSs are detected. In total, 133091 SPSs and 17630 DPSs are detected via SRN-based RNT. The heights of the detected SPSs and DPSs with SRN-based RNT are shown in Fig. 11 (left). For DPSs, only the higher scatterers corresponding to the building rooftop or façade are displayed. In the AntRN-based local star networks, 211041 SPSs and 30781 DPSs are detected. In total, 224846 SPSs and 30781 DPSs are detected via AntRN-based RNT. The heights of the detected SPSs and DPSs with the AntRN-based RNT are shown in Fig. 11 (right). In all, the number of detected PSs has increased by about 69.7% with AntRN-based RNT than with SRN-based RNT. The correctness of the estimates is validated by the smooth gradation of the estimated heights of the detected PSs and the consistency of the estimated heights of detected PSs shown in Fig. 11 (left) and Fig. 11(right).

It is seen that PSs cannot be detected with SRN-based RNT at Area 1 and Area 2 due to the lack of reference points in these two areas. But PSs can be detected with AntRN-based RNT in these two areas. In addition, the structure information of the line targets on road in Area 3 is better retrieved with AntRN-based RNT than the SRN-based RNT because more reference points are contained in this area in AntRN than in SRN. It is obvious that AntRN-based RNT has a greater ability

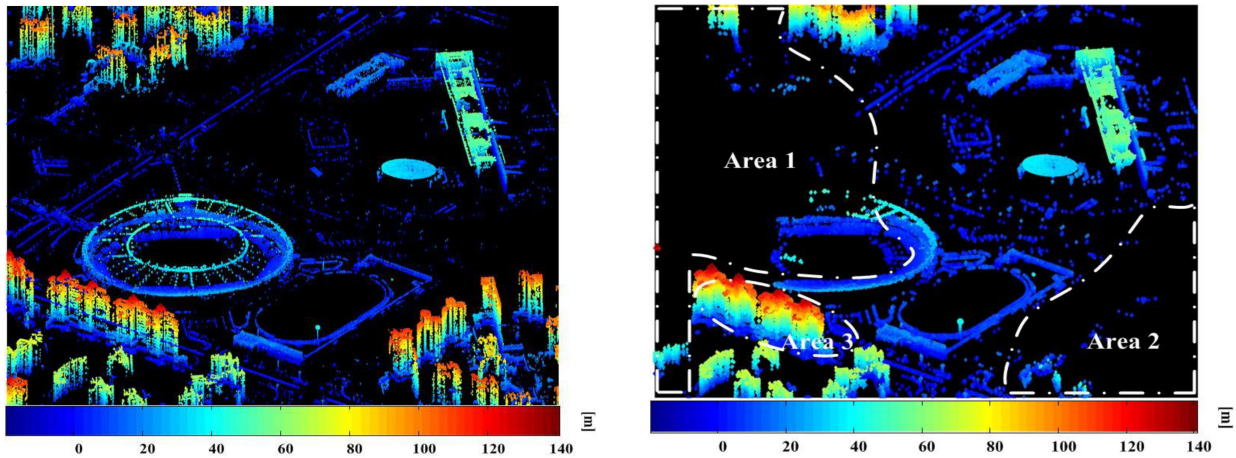

Fig. 11. Estimated heights of the detected SPSs and DPSs by SRN-based RNT (left), and AntRN-based RNT (right) with the same color bar shown in Fig. 9. For DPSs, the higher one is displayed.

for detecting PSs throughout the built scene than SRN-based RNT. This also validates that ACSA has a greater ability for constructing RN with whole-scene coverage than standard RNT.

V. Conclusion

In this article, ACSA is proposed to construct RN with global distribution throughout the whole built environment. In ACSA, reliable SPS arcs including SPSs are stepwise explored and retained to form the RN around each ant until no reliable SPSs can be explored. Therefore, the network connectivity is maintained at all times and ACSA has the capability of constructing RN with near-largest whole-scene coverage. The ACSA is a promising tool and the ACS strategy can also be applied into other fields where whole-scene network construction is needed, i.e., PSI.

Future work will focus on the following aspects.

1) Block-ACSA can be developed to improve the efficiency by constructing RN in every block and establishing reliable SPS arcs among these blocks.
2) A new algorithm can be designed with the ACS strategy for network construction in PSI.
3) The precision of retrieved height point clouds will be quantitatively evaluated by comparing the retrieved height map with the high-precision LiDAR DEM once acquired.

Acknowledgment

The authors would like to thank the German Aerospace Center (DLR) for providing the high-resolution TerraSAR-X data sets. The authors would also like to thank the anonymous reviewers for their valuable suggestions.

References

[1] J. P. Fitch, *Synthetic Aperture Radar*. New York, NY, USA: Springer-Verlag, 1988.
[2] A. Ferretti, C. Prati, and F. Rocca, "Permanent scatterers in SAR interferometry," *IEEE Trans. Geosci. Remote Sens.*, vol. 39, no. 1, pp. 8–20, Jan. 2001.
[3] B. M. Kampes, *Radar Interferometry: Persistent Scatterer Technique*. Dordrecht, The Netherlands: Springer-Verlag, 2006.
[4] M. Crosetto and O. Monserrat, "Persistent scatterer interferometry: A review," *ISPRS J. Photogramm. Remote Sens.*, vol. 115, pp. 78–89, 2005.
[5] A. Reigber and A. Moreira, "First demonstration of airborne SAR tomography using multibaseline L-band data," *IEEE Trans. Geosci. Remote Sens.*, vol. 38, no. 5, pp. 2142–2152, Sep. 2000.
[6] G. Fornaro and F. Serafino, "Imaging of single and double scatterers in urban areas via SAR tomography," *IEEE Trans. Geosci. Remote Sens.*, vol. 44, no. 12, pp. 3497–3505, Dec. 2006.
[7] X. X. Zhu, N. Adam, and R. Bamler, "First demonstration of spaceborne high resolution SAR tomography in urban environment using TerraSAR-X data," in *Proc. CEOS SAR Workshop Calibration Validation*, 2008.
[8] X. X. Zhu and R. Bamler, "Very high resolution spaceborne SAR tomography in urban environment," *IEEE Trans. Geosci. Remote Sens.*, vol. 48, no. 12, pp. 4296–4308, Dec. 2010.
[9] G. Fornaro, D. Reale, and F. Serafino, "Four-dimensional SAR imaging for height estimation and monitoring of single and double scatterers," *IEEE Trans. Geosci. Remote Sens.*, vol. 47, no. 1, pp. 224–237, Jan. 2009.
[10] X. X. Zhu, S. Montazeri, C. Gisinger, R. F. Hanssen, and R. Bamler, "Geodetic SAR tomography," *IEEE Trans. Geosci. Remote Sens.*, vol. 54, no. 1, pp. 18–35, Jan. 2016.
[11] R. Werninghaus and S. Buckreuss, "The TerraSAR-X mission and system design," *IEEE Trans. Geosci. Remote Sens.*, vol. 48, no. 2, pp. 606–614, Feb. 2010.
[12] G. Krieger *et al.*, "TanDEM-X: A satellite formation for high-resolution SAR interferometry," *IEEE Trans. Geosci. Remote Sens.*, vol. 45, no. 11, pp. 3317–3341, Nov. 2007.
[13] F. Covello, F. Battazza, and A. Coletta, "COSMO-SkyMed an existing opportunity for observing the earth," *J. Geodyn.*, vol. 49, pp. 171–180, 2010.
[14] X. X. Zhu, Y. Wang, S. Montazeri, and N. Ge, "A review of ten-year advances of multi-baseline SAR interferometry using TerraSAR-X data," *Remote Sens.*, vol. 10, no. 9, 2018, Art. no. 1374.
[15] X. X. Zhu, Z. Dong, A. X. Yu, M. Q. Wu, D. X. Li, and Y. S. Zhang, "New approaches for robust and efficient detection of persistent scatterers in SAR tomography," *Remote Sens.*, vol. 11, no. 3, 2019, Art. no. 356.
[16] R. F. Hanssen, *Radar Interferometry: Data Interpretation and Error Analysis*. Dordrecht, The Netherlands: Kluwer, 2001.
[17] E. F. Vernote and E. L. Saleous, "Atmospheric correction of MODIS data in the visible to middle infrared: First results," *Remote Sens. Environ.*, vol. 83, no. 1/2, pp. 97–111, 2002.
[18] Z. H. Li, "Correction of atmospheric water vapour effects on repeat-pass SAR interferometry using GPS, MODIS and MERIS data," Ph.D. dissertation, Dept. Geomatic Eng., Univ. London, London, U.K., 2005.
[19] M. Bevis, S. Businger, T. A. Herring, R. Rocken, R. A. Anthes, and R. H. Ware, "GPS meteorology: Remote sensing of atmospheric water vapor using the global positioning system," *J. Geophys. Res.*, vol. 97, no. D14, pp. 15787–15801, 1992.

[20] V. Janssen, L. L. Ge, and C. Rizos, "Tropospheric corrections to SAR interferometry from GPS observations," *GPS Solutions*, vol. 8, pp. 140–151, 2004.
[21] D. Perissin, E. Pichelli, R. Ferretti, F. Rocca, and N. Pierdicca, "The MM5 numerical model to correct PSInSAR atmospheric phase screen," in *Proc. FRINGE*, 2009, pp. 1–5.
[22] D. Perissin, "Mitigation of atmospheric delay in InSAR: The ESA Metawave project," in *Proc. IEEE Int. Geosci. Remote Sens. Symp.*, Jul. 2011, pp. 2558–2561.
[23] P. W. Webley, R. M. Bingley, A. H. Dodson, G. Wadge, S. J. Waugh, and I. N. James, "Atmospheric water vapour correction to InSAR surface motion measurements on mountains: Results from a dense GPS network on Mount Etna," *Phys. Chem. Earth Parts A/B/C*, vol. 27, no. 4, pp. 363–370, 2002.
[24] X. L. Ding and Z. W. Li, "Atmospheric effects on InSAR measurements and their mitigation," *Sensors*, vol. 8, no. 9, pp. 5426–5488, 2008.
[25] F. Beauducel, P. Briole, and J. L. Froger, "Volcano-wide fringes in ERS synthetic aperture radar interferograms of Etna (1992–1998): Deformation or tropospheric effect?," *J. Geophys. Res.*, vol. 105, no. B7, pp. 16391–16402, 2000.
[26] F. Sarti, H. Vadon, and D. A. Massonnet, "A method for the automatic characterization of InSAR atmospheric artifacts by correlation of multiple interferograms over the same site," in *Proc. Int. Geosci. Remote Sens. Symp.*, Jun. 1999, vol. 4, pp. 1937–1939.
[27] B. Fruneau and F. Sarti, "Detection of ground subsidence in the city of Paris using radar interferometry: Isolation of deformation from atmospheric artifacts using correlation," *Geophys. Res. Lett.*, vol. 27, no. 24, pp. 3981–3984, 2000.
[28] F. Sarti, B. Fruneau, and T. Cunha, "Isolation of atmospheric artifacts in differential interferometry for ground displacement detection: Comparison of different methods," in *Proc. Eur. Space Agency ERS-Envisat Symp.*, Dec. 2001.
[29] Z. Hu, J. J. Mallorquí, and H. Fan, "Atmospheric artifacts correction with a covariance-weighted linear model over mountainous regions," *IEEE Trans. Geosci. Remote Sens.*, vol. 56, no. 12, pp. 6995–7008, Dec. 2018.
[30] P. F. Ma and H. Lin, "Robust detection of single and double persistent scatterers in urban built environment," *IEEE Trans. Geosci. Remote Sens.*, vol. 54, no. 4, pp. 2124–2139, Apr. 2016.
[31] P. F. Ma and H. Lin, "Multi-dimensional SAR tomography for monitoring the deformation of newly built concrete buildings," *ISPRS J. Photogramm. Remote Sens.*, vol. 106, pp. 118–128, 2015.
[32] X. X. Zhu and R. Bamler, "Tomographic SAR inversion by L1-norm regularization—The compressive sensing approach," *IEEE Trans. Geosci. Remote Sens.*, vol. 48, no. 10, pp. 3839–3846, Oct. 2010.
[33] G. Fornaro, F. Lombardini, A. Pauciullo, D. Reale, and F. Viviani, "Tomographic processing of interferometric SAR data: Developments, applications, and future research perspectives," *IEEE Signal Process. Mag.*, vol. 31, no. 4, pp. 41–50, Jul. 2014.
[34] A. De Maio, G. Fornaro, and A. Pauciullo, "Detection of single scatterers in multidimensional SAR imaging," *IEEE Trans. Geosci. Remote Sens.*, vol. 47, no. 7, pp. 2284–2297, Jul. 2009.
[35] A. Pauciullo, D. Reale, A. De Maio, and G. Fornaro, "Detection of double scatterers in SAR tomography," *IEEE Trans. Geosci. Remote Sens.*, vol. 50, no. 9, pp. 3567–3586, Sep. 2012.
[36] M. A. Siddique, U. Wegmüller, I. Hajnsek, and O. Frey, "Single-look SAR tomography as an add-on to PSI for improved deformation analysis in urban areas," *IEEE Trans. Geosci. Remote Sens.*, vol. 54, no. 10, pp. 6119–6137, Oct. 2016.
[37] H. Luo, Z. Dong, A. X. Yu, Y. S. Zhang, and X. X. Zhu, "Super-resolved multiple scatterers detection in SAR tomography based on compressive sensing generalized likelihood ratio test (CS-GLRT)," *Remote Sens.*, vol. 11, no. 16, 2019, Art. no. 1930.
[38] X. X. Zhu and R. Bamler, "Super-resolution power and robustness of compressive sensing for spectral estimation with application to spaceborne tomographic SAR," *IEEE Trans. Geosci. Remote Sens.*, vol. 50, no. 1, pp. 247–258, Jan. 2012.
[39] K. P. Burnham and D. R. Anderson, "Multimodel inference: Understanding AIC and BIC in model selection," *Sociol. Methods Res.*, vol. 33, no. 2, pp. 261–304, 2004.
[40] M. Dorigo, M. Birattari, and T. Stutzle, "Ant colony optimization," *IEEE Comput. Intell. Mag.*, vol. 1, no. 4, pp. 28–39, Nov. 2006.
[41] J. L. Bentley, "Fast algorithms for geometric traveling salesman problems," *ORSA J. Comput.*, vol. 4, no. 4, pp. 387–411, 1992.
[42] L. Bianchi, L. M. Gambardella, and M. Dorigo, "Solving the homogeneous probabilistic traveling salesman problem by the ACO metaheuristic," in *Proc. 3rd Int. Workshop Ant Algorithms*, Sep. 2002, pp. 176–187.
[43] B. Bullnheimer, R. F. Hartl, and C. Strauss, "An improved Ant system algorithm for the vehicle routing problem," *Ann. Oper. Res.*, vol. 89, no. 1, pp. 319–328, 1999.
[44] M. Reimann, K. Doerner, and R. F. Hartl, "D-Ants: Savings based ants divide and conquer the vehicle routing problem," *Comput. Oper. Res.*, vol. 31, no. 4, pp. 563–591, 2004.
[45] P. Toth and D. Vigo, *The Vehicle Routing Problem Discrete Math (Siam Monographs on Discrete Mathematics and Applications)*, vol. 94, no. 2/3. Philadelphia, PA, USA: SIAM, 2001, pp. 127–153.
[46] G. D. Caro and M. Dorigo, "Ant colonies for adaptive routing in packet-switched communications networks," in *Proc. Int. Conf. Parallel Problem Solving Nature*, Jun. 2000, pp. 673–682.
[47] G. D. Caro, F. Ducatelle, and L. M. Gambardella, "AntHocNet: An ant-based hybrid routing algorithm for mobile ad hoc networks," *Euro Trans. Telecom.*, vol. 3242, pp. 461–470, 2004.
[48] G. Liu, S. M. Buckley, X. Ding, Q. Chen, and X. Luo, "Estimating spatiotemporal ground deformation with improved permanent-scatterer radar interferometry," *IEEE Trans. Geosci. Remote Sens.*, vol. 47, no. 8, pp. 2762–2772, Aug. 2009.

Yang Huang received the B.S. degree in observation and control technology and instrument from the Xi'an University of Posts & Telecommunications, Hangzhou, China, in 2013, and the M.S. degree in information and communication engineering from Air Force Engineering University, Xi'an, China, in 2016. He is currently working toward the Ph.D. degree in information and communication engineering with the National University of Defense Technology, Changsha, China.

His major research interests include radar signal processing, digital beamforming, and synthetic aperture radar tomography.

Xiaoxiang Zhu was born in Nantong, Jiangsu, China, in 1992. He received the B.S. degree in electronic information engineering from the Nanjing University of Science and Technology, Nanjing, China, in 2014, and the Ph.D. degree in information and communication engineering from the National University of Defense Technology, Changsha, China, in 2021.

Xiantao Wang was born in Rizhao, Shangdong, China, in 1996. He received the B.S. degree in electronic information engineering from Tsinghua University, Beijing, China, in 2018. He is working toward the Ph.D. degree in information and communication engineering with the College of Electronic Science and Technology, National University of Defense Technology, Changsha, China.

His major research interests include radar signal processing and synthetic aperture radar tomography. His research fields of interest include radar signal processing, synthetic aperture radar, and synthetic aperture radar tomography.

Zhen Dong was born in Anhui, China, in September 1973. He received the Ph.D. degree in electrical engineering from the National University of Defense Technology (NUDT), Changsha, China, in 2001.

He is currently a Professor with the School of Electronic Science and Engineering, NUDT. His recent research interests include synthetic aperture radar system design and processing, ground moving target indication, and digital beamforming.

Anxi Yu was born in Henan, China, in 1978. He received the Ph.D. degree in information and communication engineering from the National University of Defense Technology, Changsha, China, in 2003.

He is currently an Associate Professor with the School of Electronic Science, National University of Defense Technology. His research interests include spaceborne interferometry synthetic aperture radar signal processing, signal simulation, and system technology.